RSC Advances

PAPER

View Article Online
View Journal | View Issue

Cite this: *RSC Adv.*, 2020, **10**, 3861

Measuring nanoparticle-induced resonance energy transfer effect by electrogenerated chemiluminescent reactions†

Pilar Perez-Tejeda,*[a] Alberto Martínez-Delgado,[a] Elia Grueso[a] and Rosa M. Giráldez-Pérez[ab]

Received 28th October 2019
Accepted 18th December 2019

DOI: 10.1039/c9ra08857a

rsc.li/rsc-advances

Electrogenerated chemiluminescence (ECL) efficiencies, redox potentials, photoluminescent (PL) (quenching and coupling) effects, and AFM images for the $[Ru(bpy)_3]^{2+}$/Au@tiopronin system were determined in aqueous solutions of the gold nanoparticles (NPs) at pH 7.0. The most remarkable finding was that ECL measurements can display the nanoparticle-induced resonance energy transfer (NP-RET) effect. Its effectiveness was quantified through a coefficient, $K_{(NP\text{-}RET)_{ECL}}$, which measures how much an ECL reaction has been enhanced. Moreover, the NP-RET effect was also checked using PL measurements, in such a way that a coefficient, $K_{(NP\text{-}RET)_{PL}}$, was determined; both constants, $K_{(NP\text{-}RET)_{ECL}}$ and $K_{(NP\text{-}RET)_{PL}}$ being in close agreement. It is important to highlight the fact that the NP-RET effect is only displayed in diluted solutions in which there is no NPs self-aggregation. The existence of the NPs self-aggregation behavior is revealed through AFM measurements.

1. Introduction

In a broad sense relevant aspects of non-covalent interactions in supramolecular systems can be studied using the Förster resonance energy transfer (FRET) approach.[1–8] In this type of energy transfer process an excited donor fluorophore (dye) transfers its energy to an acceptor molecule, which normally relaxes by emitting light if it is photoluminescent (PL); if this species is not itself PL, then there is a quenching effect. Certain requirements must be met for the process to take place.[5–7] First, sufficient spectral overlap is required between the emission donor and absorption acceptor species.[5] Second, the distance between the molecules must be less than approximately 10 nm.[6] Finally, the fluorophores should be conveniently oriented with respect to each other.[7] In fact, FRET efficiency depends on these three factors, and is highly sensitive to the donor–acceptor distance (R). Therefore, using the concept of FRET coupling, quantitative information can be obtained about several relevant characteristics of supramolecular phenomena.[8]

However, a major limitation of FRET interactions is the relatively small distance ($\approx$10 nm) at which the energy can be transferred. There are several ways to resolve this situation. One of these comprises the formation of cascades, in which several FRET fluorophores with increasingly longer excitation wavelengths are organized in devices to facilitate energy transfer over distances greater than 10 nm or more.[9–11] Efforts made in this regard, outside the regime of interaction between point dipoles, are also important. That is, resonance energy transfer (RET) efficiency has been predicted based on R^{-4} or R^{-2} donor–acceptor distance dependence[12–14] and not on R^{-6} (Förster theory). Thus, the energy can be transferred over a distance of 20 nm from an organic dye to a spherical metal nanoparticle (NP) which acts as a surface better than a point dipole.[15] Currently, FRET is being replaced by plasmon-enhanced or metal-induced resonance energy transfer, which as demonstrated can work at distances of up to 100 nm.[15–18] Therefore, the challenge now is to use metal NPs for the study of non-covalent interactions in supramolecular media using FRET or plasmon-enhanced techniques.

In addition, the study of the plasmon–molecule interaction is gaining increasing attention.[4,19–21] In point of fact, the enhancement of photoluminescence (PL) by a nanoparticle uses in an effective way the coupling between excited dyes and the localized surface plasmon resonance (SPR) in metal nanostructures in an effective way. This interaction effect has contributed to the development of nanotechnology:[22–27] for instance, solar energy storage and conversion[22–24] and optical biosensing,[25–27] rely on this type of the energy transfer.

Based on the preceding results, the subject of plasmon–molecule couplings is of interest because the understanding of these interactions can help address important issues related to the potential applications of nanomaterials and supramolecular media. The aim of this study is to obtain a deeper insight

[a]Department of Physical Chemistry, Faculty of Chemistry, University of Sevilla, C/Profesor García González, 1, 41012, Sevilla, Spain. E-mail: pptejeda@us.es
[b]Department of Cellular Biology, Physiology and Immunology, University of Córdoba, Spain

† Electronic supplementary information (ESI) available. See DOI: 10.1039/c9ra08857a

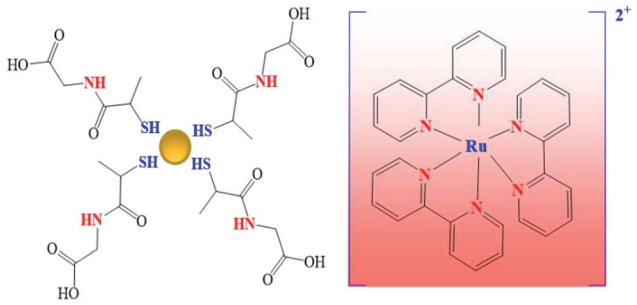

Scheme 1 Au@tiopronin/$[Ru(bpy)_3]^{2+}$ system.

into the plasmon–molecule interactions using a high-energy electrogenerated chemiluminescent (ECL) reaction in colloidal gold solutions. ECL is a process that follows several fundamental pathways. In the first step, an electrode originates species that in successive paths will give rise to high-energy electron–transfer reactions in solution, which in turn will produce one or two species in their excited state.[28–37]

After about 50–60 years of study, ECL has proven to be a useful research tool in a wide variety of areas.[31–39] Indeed, there are studies in which the increase in ECL due to the coupling between plasmons and dyes is applied to the detection of different species.[38–42] These studies have contributed to the development of the ECL reactions as an analytical technique, given their significant impact. However, to our knowledge, there are few studies in which the magnitude of the coupling effect is quantified.[43]

To study plasmon–molecule interactions was used the ECL reaction, $[Ru(bpy)_3]^{2+}$ + $C_2O_4^{2-}$, in the presence of several Au@tiopronin‡ NPs (see Scheme 1) aqueous solutions. In addition, photoluminescent (PL) (quenching and coupling) of the $[Ru(bpy)_3]^{2+}$* species as well as atomic force microscopy (AFM) measurements were carried out; redox potentials of the $[Ru(bpy)_3]^{3+/2+}$ couple were also determined in several NP solutions. The noteworthy findings were that ECL measurements can display the emission-dye-NPs coupling effect or as we have called it, the nanoparticle-induced resonance energy transfer (NP-RET) effect, and it is also possible to quantify its effectiveness. A coefficient was defined which measures the efficiency that a given system of NPs has for the improvement of ECL in a particular reaction. Specifically, this coefficient measures how much an ECL reaction is improved by the NP-RET effect. The novelty here lies in using an ECL reaction as a technique to measure the NP-RET efficiency of a dye-NP system and confirm its value *via* photoluminescence measurements. All experiments were carried out at pH 7.0 and 298.15 ± 0.01 K.

‡ The gold clusters protected with tiopronin are NPs of alkanethiolate in which the presence of a carboxylic and an amino group on the tiopronin can modify the charge of the particles depending on the medium's pH. Consequently, this colloidal system offers the possibility of being positively or negatively charged. In fact, at $pK_a \approx 5.6$, Au@tiopronin nanoparticles are commonly neutral and hydrophilic.[44,45] Thus, at pH 7.0, for example, the Au@tiopronin NPs will be negatively charged. The judicious choice of the medium pH will determine not only how these NPs interact with the surrounding solvent molecules but also the aggregation of the nanoparticles themselves.[46] In order to minimize the self-aggregation, the medium pH chosen was 7.0.

2. Materials and methods

2.1. Materials

All chemicals $[Ru(bpy)_3]Cl_2$, $Na_2C_2O_4$, $CH_3AsO_2Na3H_2O$ (cacodylate), NaCl, HCl, *N*-(2-mercaptopropionyl)glycine (tiopronin), $HAuCl_43H_2O$, MeOH, CH_3COOH and $NaBH_4$ were analytical grade, purchased from Sigma-Aldrich and used without further purification. Gold nanoparticles were synthetized following the method of Templeton *et al.*[45] Dialysis sacks 25EA from Sigma were utilized for purification of the gold nanoparticles. These were characterized by UV-visible absorption spectra (*vide infra*) (Fig. 1), TEM microscopy (*vide infra*) (Fig. 2) and C, H, N, and S microanalysis (11.80% C; 1.86% H; 2.89% N; 7.37% S). From gold core size distribution (see Fig. 2) the average size of Au colloids was 3.3 ± 0.5 nm. Accordingly, the relation between the number of Au atoms and tiopronin ligands[45] was 314/101. Consequently, the molecular weight calculated for $C_{505}H_{909}O_{303}N_{101}S_{101}Au_{314}$ was 79 680 g mol^{-1}. All the solutions were prepared with deionized water obtained from a Millipore Milli-Q system, having a conductivity less than $<10^{-6}$ S m^{-1}. All experiments were carried out with Au colloid solutions prepared by weight.

2.2. Electrogenerated chemiluminescence measurements

ECL measurements (cyclic voltammetry (CV) experiments plus ECL emissions) were carried out as in previous works.[47–49] All ECL measurements were recorded using the CV technique working at a scan rate of 100 mV s^{-1}. The uncertainty of the relative measured ECL efficiency (Φ_{ECL}) (see Section 3.1) was less than 4% from the average of two or three measurements in

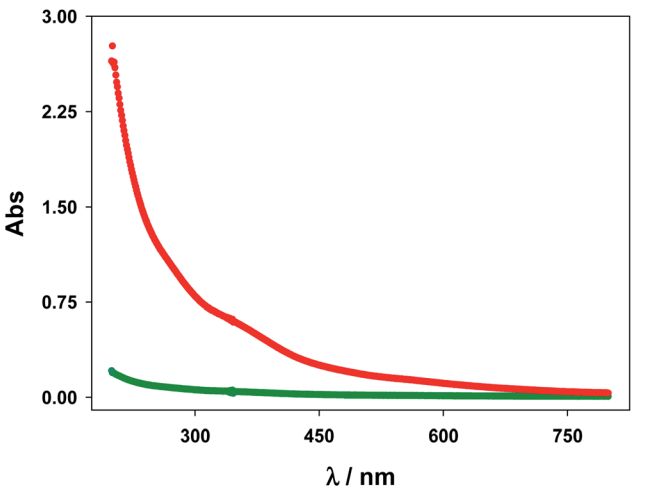

Fig. 1 UV-visible absorption spectra of the Au@tiopronin nanoparticles in the absence of the $[Ru(bpy)_3]^{2+}$ species and presence of the cacodylate buffer, pH 7.0 (*vide infra*). Green and red lines denote 2.0 × 10^{-7} M and 2.0 × 10^{-6} M [Au@tiopronin]. As can be seen, a slight but detectable surface plasmon band (SPR) appears as a consequence of the small size of nanoclusters when the [Au@tiopronin] increases.

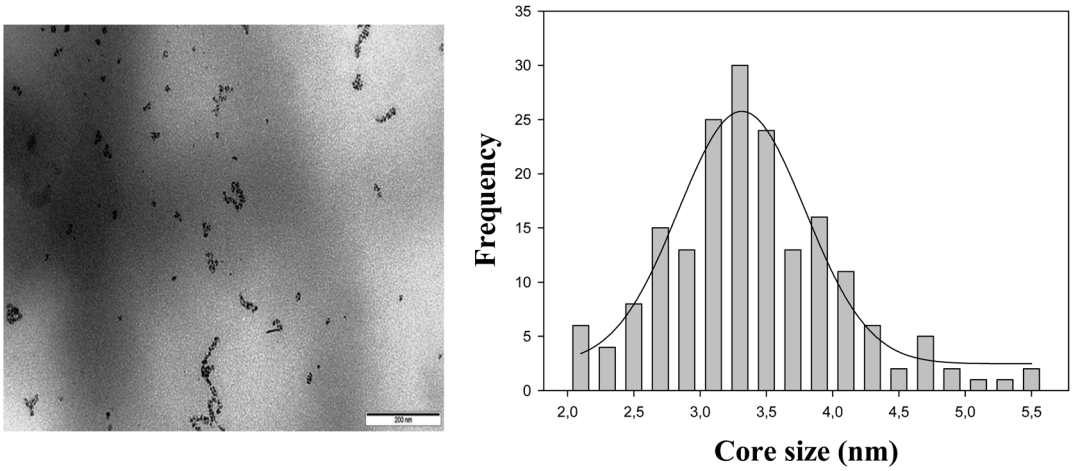

Fig. 2 TEM image (left) and size distribution (right) of the tiopronin gold nanoparticles in the absence of the Ru(II) complex and presence of the cacodylate buffer at pH 7.0.

four scans, after system calibration. ECL measurements were taken for several AuNPs solutions (from 1.00×10^{-8} M to 1.00×10^{-6} M (see Table 1)). 2.0×10^{-4} M and 2.0×10^{-3} M were always the concentrations of $[Ru(bpy)_3]^{2+}$ and $C_2O_4^{2-}$, respectively. All experiments were carried out at pH 7.0 by using a buffer 3.0×10^{-2} M $NaCH_3AsO_2$/3.8×10^{-3} M HCl plus 6.6×10^{-3} M NaCl. In this way, the ionic strength was also fixed at 0.040 M in each solution.

2.3. Electrochemical measurements

Peak potentials (E_{peak}) for the $[Ru(bpy)_3]^{3+/2+}$ couple in several AuNPs solutions were determined using the differential pulse voltammetry (DPV) technique, as in previous works.[47–49] The experimental conditions were identical with those corresponding to ECL measurements (*vide supra*).

Table 1 Relative ECL efficiencies (Φ_{ECL}), integrated charges (Q) and integrated ECL emission intensities (I_{ECL}) for $[Ru(bpy)_3]^{2+}$ + $C_2O_4^{2-}$ reaction, and redox potentials (E_{peak}) of the $[Ru(bpy)_3]^{3+/2+}$ couple for several Au@tiopronin nanoparticle solutions[a]

10^8 × [AuNPs]/M	$10^2 \times \Phi_{ECL}$	$10^3 \times Q$/C	$10^{-6} \times I_{ECL}$/counts	E_{peak}/V
0.00	3.85	0.149	0.304	1.092
1.00	4.55	0.341	0.341	1.097
3.00	5.23	0.483	0.587	1.112
4.00	5.81	0.453	0.609	1.087
5.00	6.22	0.404	0.641	1.082
5.50	5.78	0.339	0.497	1.087
6.00	4.98	0.326	0.414	1.092
7.00	4.46	0.395	0.426	1.095
8.00	3.39	0.341	0.267	1.097
10.0	2.74	0.366	0.257	1.092
13.0	2.95	0.309	0.239	1.107
40.0	2.35	0.360	0.218	1.106
50.0	2.51	0.320	0.194	1.112
100	2.49	0.310	0.199	1.115

[a] pH 7.0, cacodylate buffer ($[NaCH_3AsO_2] = 3.0 \times 10^{-2}$ M, $[HCl] = 3.8 \times 10^{-3}$ M), 6.2×10^{-3} M NaCl. Ionic strength 0.040 M.

2.4. Spectroscopic measurements

A Cary 500 Scan UV-vis-NIR spectrophotometer was used to record the absorption spectra of the AuNP solutions. Fig. 1 shows characteristic UV-vis spectra of some Au@tiopronin solutions as an example. As can be seen a slight detectable surface plasmon band (SPR) appears as a consequence of the small size of nanoclusters.

Photoluminescent spectra for the $[Ru(bpy)_3]^{2+*}$ excited species were acquired with a Photon Technology International (PTI). Several sets of experiments were carried out in the presence of the cacodylate buffer at pH 7.0. To study the quenching effect (see Section 3.4) in the first set of experiments, the excitation wavelength was that corresponding to the absorption maximum (454 nm), whereas in the second set of experiments it was 500 nm, the one corresponding to an absorbance of 0.2. The concentrations of the $[Ru(bpy)_3]^{2+}$ complex were 2.0×10^{-6} M and 2.0×10^{-4} M, respectively. To study the coupling effect (see Section 3.5) the excitation wavelength was 454 nm and 4.0×10^{-7} M $[Ru(bpy)_3]^{2+}$.

2.5. Transmission electronic microscopy (TEM) measurements

TEM analysis was carried out using a Philips CM 200 electron microscope working at 200 kV. 10 μL of the AuNPs aqueous solution was placed on a copper grid coated with a carbon film. The grid was left to air dry for several hours at room temperature. The solutions were prepared in the absence of the Ru(II) complex and presence of the cacodylate buffer at pH 7.0 (see Fig. 2).

2.6. Atomic force microscopy (AFM) measurements

Images were obtained with a Molecular Imaging PicoPlus 2500 AFM (Agilent Technologies). Silicon cantilevers (Model

Pointprobe, Nanoworld) with a resonance frequency of around 240 kHz and nominal force constant of 42 N m^{-1} were used. All AFM images were recorded in air and in tapping mode, with scan speeds of about 0.5 Hz and data collection at 256 × 256 pixels. At least two mica specimens were prepared for each solution, and at least 6 distinct areas of each specimen were investigated using the sample probe tip. The solutions were prepared in the absence and presence of 2.0 × 10^{-4} M $[Ru(bpy)_3]^{2+}$ complex and 2.0 × 10^{-3} M $C_2O_4^{2-}$ plus cacodylate buffer at pH 7.0 plus the suitable [AuNP].

100 μL of solutions was dropped onto a mica surface and adsorbed for 30 min in a humidified chamber. Following incubation, samples were washed with ultra-pure water and subsequently air dried for AFM imaging. In order to prevent the formation of salt crystals on the mica surface, the rinse was performed without cacodylate buffer.

3. Results

3.1. Electrogenerated chemiluminescence

In order to determine the ECL efficiency values (*vide infra*) the ECL emission-time and current-time curves corresponding to a given CV voltammogram were obtained. Fig. 3 shows a set of experimental measurements generated *via* CV as an example: current-time curves for $[Ru(bpy)_3]^{3+/2+}$ couple (top) and their corresponding ECL intensity-time curves for $[Ru(bpy)_3]^{2+*}$ excited state (bottom), (see also Fig. S1† (ECL spectrum) and Fig. S2† (CV voltammogram) in ESI†). Of course, background experiments were done for all cases, whereas ECL emissions were irrelevant, the current-time curves of the backgrounds for all the measurements were taken into account when calculating ECL efficiency values.

The ECL emission efficiency or ECL quantum yield (Φ_{ECL}) (emitted photon per transferred proton) can be approximately defined by the coulometric efficiency by:[50–52]

$$\Phi_{ECL} = \frac{\int_0^t I_e dt}{\int_0^t i dt \left(\frac{N_A}{F}\right)} \quad (1)$$

where I_e and i are the intensity in photons per second and the current in amperes (coulombs per second), respectively, integrated over a finite period of time, t. F and N_A are the Faraday and Avogadro constants, respectively. As an alternative, a standard reaction is often used, simplifying both the experimental measurements and the calculation of Φ_{ECL}:[47–49]

$$\Phi_{ECL} = \Phi^o_{ECL} \frac{Q^o I_{ECL}}{Q I^o_{ECL}} \quad (2)$$

where Q and Q^o are the integrated charge for the actual and standard reactions, respectively; I_{ECL} and I^o_{ECL} are the integrated photon intensities for both cases. Φ^o_{ECL} is the ECL efficiency in the absence of Au@tiopronin nanoparticles for a standard reaction ($[Ru(bpy)_3]^{2+}$ + $C_2O_4^{2-}$ in 0.01 M phosphate buffer (pH 6.1) + 0.1 M NaCl)[53] equal to 0.0185 at 298.15 K.[47] Relative ECL efficiency values were determined by means of eqn (1) and (2) for all NP solutions; the results are given in Table 1.

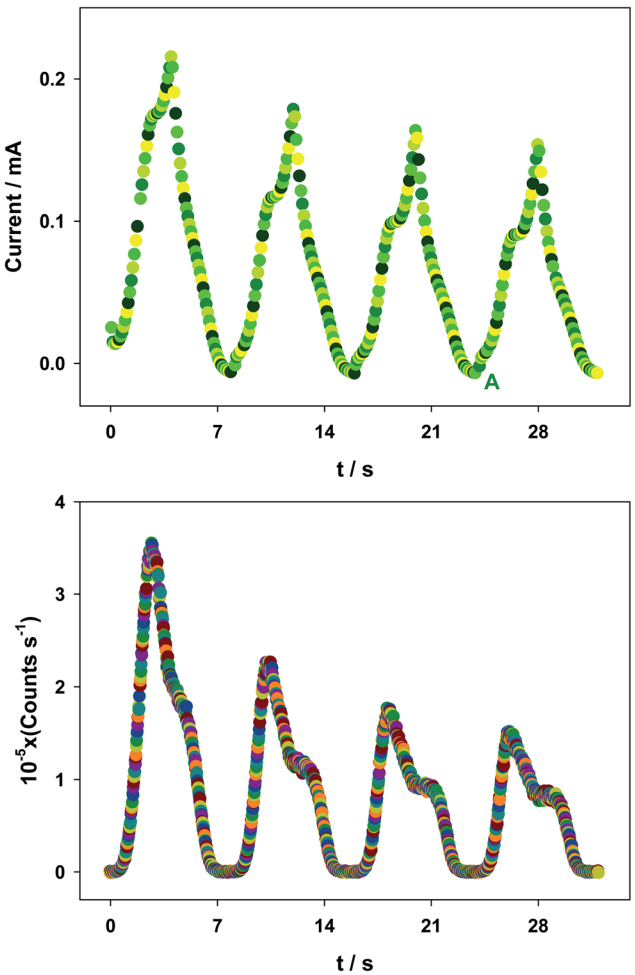

Fig. 3 Current (top) and ECL intensity (bottom) as functions of time in a CV measurement of four scans for the $[Ru(bpy)_3]^{2+}$ + $C_2O_4^{2-}$ reaction in 5.0 × 10^{-8} M AuNPs. Scan rate: 100 mV s^{-1}. Cacodylate buffer (pH 7.0). Ionic strength 0.040 M.

3.2. Redox potentials

In order to obtain some information about the microenvironment around the $[Ru(bpy)_3]^{2+}$ complex, redox potentials were evaluated. The DPV technique was used to determine the redox potential values by means of eqn (3), which relates the peak and half-wave potentials for a reversible system:

$$E_{peak} = E_{1/2} \pm \Delta E/2 \quad (3)$$

where ΔE is the pulse voltage amplitude (2.5 mV in our experiments) and the signs ± denote anodic or cathodic scans, thus $E_{peak} \approx E_{1/2}$, resulting, their uncertainty in the values measured being about ±3 mV. Fig. 4 illustrates a typical DPV voltammogram as an example. The results of redox potentials are collected in Table 1. As can be seen there is no significant variation in the values of the redox potentials. This fact seems to indicate that the addition of increasing amounts of nanoparticles does not affect the environment surrounding the $[Ru(bpy)_3]^{3+/2+}$ couple. This feature seems to show that the electric field created by the charged NPs is very weak and,

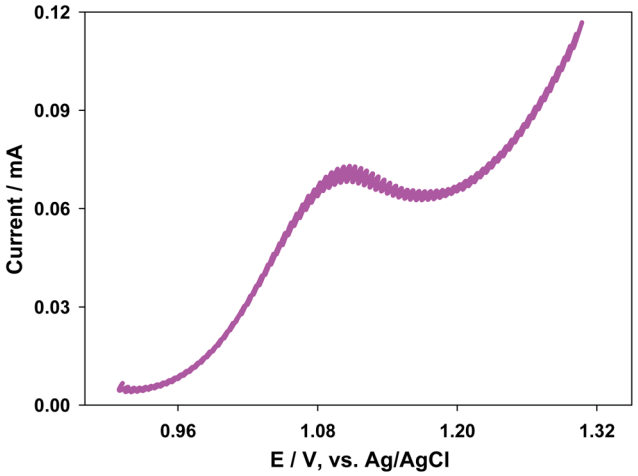

Fig. 4 Differential pulse voltammogram for the $[Ru(bpy)_3]^{3+/2+}$ couple in the presence of 7.0×10^{-8} M [AuNPs]. Cacodylate buffer (pH 7.0). Ionic strength 0.040 M.

consequently, the variation of the interaction between NPs and the Ru(II) and Ru(III) species is not significant.

3.3. Self-aggregation performance

In order to rationalize the trends of Φ_{ECL}/[AuNPs] self-aggregation measurements were necessary. To this end, AFM method was carried out. Fig. S3† (bottom) and 5 display AFM images for 8.0×10^{-8} M [AuNPs] in the absence and presence of 2.0×10^{-4} M $[Ru(bpy)_3]^{2+}$, respectively. Likewise, Fig. S3† (top) and 6 show the images at 1.0×10^{-8} M [AuNPs].

Comparison between Fig. 5 and 6 allowed us to verify the self-aggregation of particles. As can be seen in Fig. 5 when the concentration is 8.0×10^{-8} M, large aggregates can be distinguished. However, in the case of solutions at 1.0×10^{-8} M [AuNPs], aggregation does not seem to occur (Fig. 6). In addition, the Ru(II) complex induced the formation of more aggregates (see Fig. S3† (top and bottom)), but this does not determine their formation in any of the cases. That is to say, at 1.0×10^{-8} M [AuNPs], in the absence or presence of the Ru(II) complex there is no aggregation (see Fig. S3† (top) and 6). For both histograms (see Fig. 5 and 6), the average diameters of NPs at 8.0×10^{-8} M and 1.0×10^{-8} M [AuNPs] were 8.6 ± 0.9 nm and 3.7 ± 0.6 nm, respectively. Comparison between them allows us to discover which monomers on average form a NP self-aggregate, $n = 2.3 \pm 0.6$.

3.4. Quenching effect

To verify whether the quenching effect was at work or not under our experimental conditions, the photoluminescent spectra of the $[Ru(bpy)_3]^{2+}$* species were recorded for the whole concentration range of AuNPs (see Table 1). Fig. S4A† displays some spectra as examples (see ESI† for details). Bear in mind that there is no significant quenching effect in diluted solutions. For this reason, the [AuNP] was increased up to 2.0×10^{-6} M.

The Stern–Volmer approach can be applied in order to take into account the magnitude of the quenching effect:

$$\left(\frac{I_o}{I}\right)_{PL} = 1 + (K_D + K_S)[\text{AuNPs}] \quad (4)$$

where K_D and K_S are the dynamic and static quenching constants, respectively, [AuNPs] is the [quencher], and $(I_o/I)_{PL}$ the emission ratio for Ru(II)* species (with I_o and I having their usual meaning). Eqn (4), which predicts a linear relationship between [AuNPs] and $(I_o/I)_{PL}$, is fulfilled as shown in Fig. 7, from which slope $K_Q = (K_D + K_S)$ was calculated, being equal to 4.5×10^5 M^{-1}. Notice that if the concentration of NPs is further increased up to 4.0×10^{-6} M a Stern–Volmer quadratic equation taking into account static (K_S) and dynamic (K_D) quenching constants may be operative (see eqn (1S), Fig. S4B and S5†). However, although the fit between experimental data and eqn (1S)† is good the results for K_S and K_D are not consistent. This behavior could be due to the formation of self-aggregates, which seems be more significant when the concentration of the AuNPs increases as demonstrated previously (see Section 3.3).

3.5. Coupling effect

Another set of photoluminescent spectra was recorded to ascertain whether the photoluminescent intensity of the $[Ru(bpy)_3]^{2+}$* species increases or not in the presence of the Au@tiopronin particles at a range of diluted concentrations. These spectra were carried out at 1.0×10^{-8} M and 8.0×10^{-8} M [AuNPs] under buffer conditions (pH 7.0) at 4.0×10^{-7} M $[Ru(bpy)_3]^{2+}$. Fig. 8 clearly shows that the photoluminescent intensity of the $[Ru(bpy)_3]^{2+}$* species increases at the diluted solutions of the NPs, which is not so for the concentrated solutions (see Fig. S6†). For the latter solutions, a slight decay of light intensity is observed.

4. Discussion

As shown in Table 1, Φ_{ECL} values increase up to approximately 5.00×10^{-8} M [AuNPs] and then Φ_{ECL} values decrease. In order to explain this particular Φ_{ECL}-[AuNP] trend, redox potentials, quenching and coupling effects together with AFM photograms were measured for gold nanocluster solutions. However, before continuing, an explanation from a qualitative point of view concerning the trends of Φ_{ECL}, I_{ECL} and Q among one another seems pertinent.

It is clear from Table 1 that the integrated charge of Au@tiopronin nanoparticles increases about 2.7-fold its value when the [AuNPs] increase up to about 5.0×10^{-8} M, in relation to that in the absence of NPs. In this same range of concentrations, Φ_{ECL} values increase 1.6-fold, whereas integrated ECL emission shows an enhancement of about 2.1-fold in comparison with its value in the absence of AuNPs. Hence, the increase in ECL efficiency is due to the augmentation of the ECL emission intensity at the 0.0–5.00×10^{-8} M NPs concentration range.

Subsequently, from [AuNPs] > 5.00×10^{-8} M, both Φ_{ECL} and ECL emission intensity follow the same tendencies; they decrease when NP content increases (see Table 1). Notice that the increase in the amount of NPs from 5.00×10^{-8} M does not produce any variation in the Q values, which remain nearly

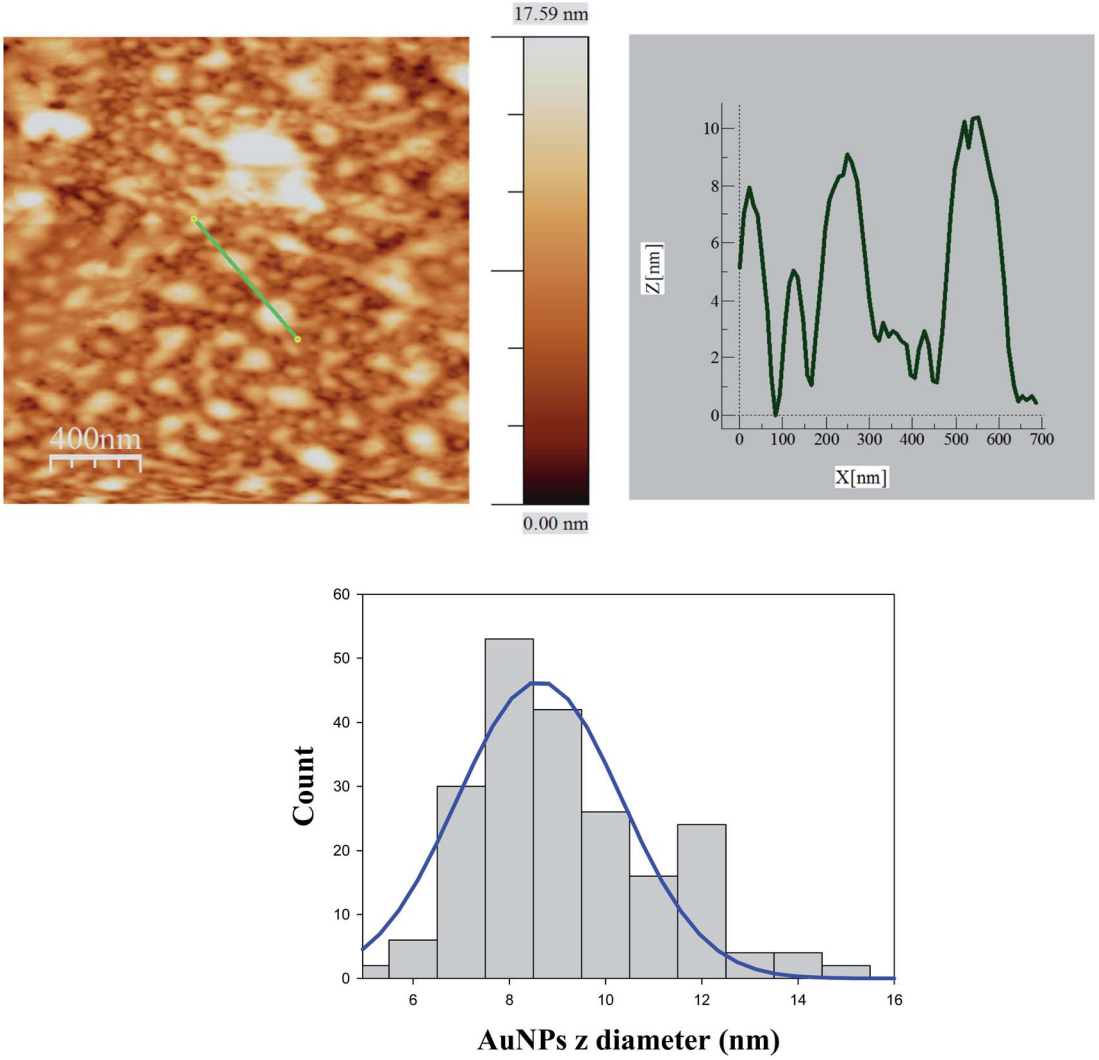

Fig. 5 AFM image for 8.0×10^{-8} M [Au@tiopronin] in the presence of $[Ru(bpy)_3]^{2+}$ and corresponding histogram from which the average diameter obtained was 8.6 ± 0.9 nm.

constant within the experimental uncertainty ($Q = (0.37 \pm 0.06) \times 10^{-3}$ C). This behavior may be a consequence of the formation of self-aggregates when increasing the concentration of NPs. That is, the addition of charged Au@tiopronin species in sufficient quantity would result, on average, in the neutralization of the monomers therein. Therefore, the Φ_{ECL}-[AuNPs] trend is determined to a considerable extent by the I_{ECL}-[AuNPs] trend.

In keeping with the preceding discussion, Φ_{ECL} behavior is worthy of consideration, taking into account two ranges of concentrations: one diluted, up to $\approx 5.00 \times 10^{-8}$ M [AuNPs], and another concentrated from $\approx$ the previous value of [AuNPs]. These two ranges of NP concentrations will be treated below in this way: diluted and concentrated ranges.

As mentioned above, by means of the redox potential variation as a function of a particular medium content, it is possible to obtain information about the microenvironment that, on average, would have a redox couple around it. In line with this idea, the redox potentials of the $[Ru(bpy)_3]^{3+/2+}$ couple were determined, and the results are summarized in Table 1 (see Section 3.2). These results show that the addition of increasing amounts of nanoparticles does not affect the environment surrounding the couple $[Ru(bpy)_3]^{3+/2+}$ (see Section 3.2), which seems to corroborate the previous discussion about the dominance of I_{ECL} on the integrated charge.

As aforesaid, the trend of ECL efficiency is governed by that of the ECL emission intensity. In addition, Section 3.3 shows that under our experimental conditions the Au@tiopronin system suffers self-aggregation at the concentrated range of the [AuNPs], whereas at the dilute range of NP concentrations there are no aggregates in either the presence or absence of the Ru(II) complex. Therefore, both light emission and self-aggregation will allow us to rationalize the Φ_{ECL}-[AuNP] trend.

In effect, from a qualitative point of view, it is easy to understand that both the quenching effect and the NP self-aggregation would reduce I_{ECL}, and, therefore, Φ_{ECL}, and that these effects would be rendered more efficient by increasing the NPs concentration. Nevertheless, in the diluted range of NPs, an

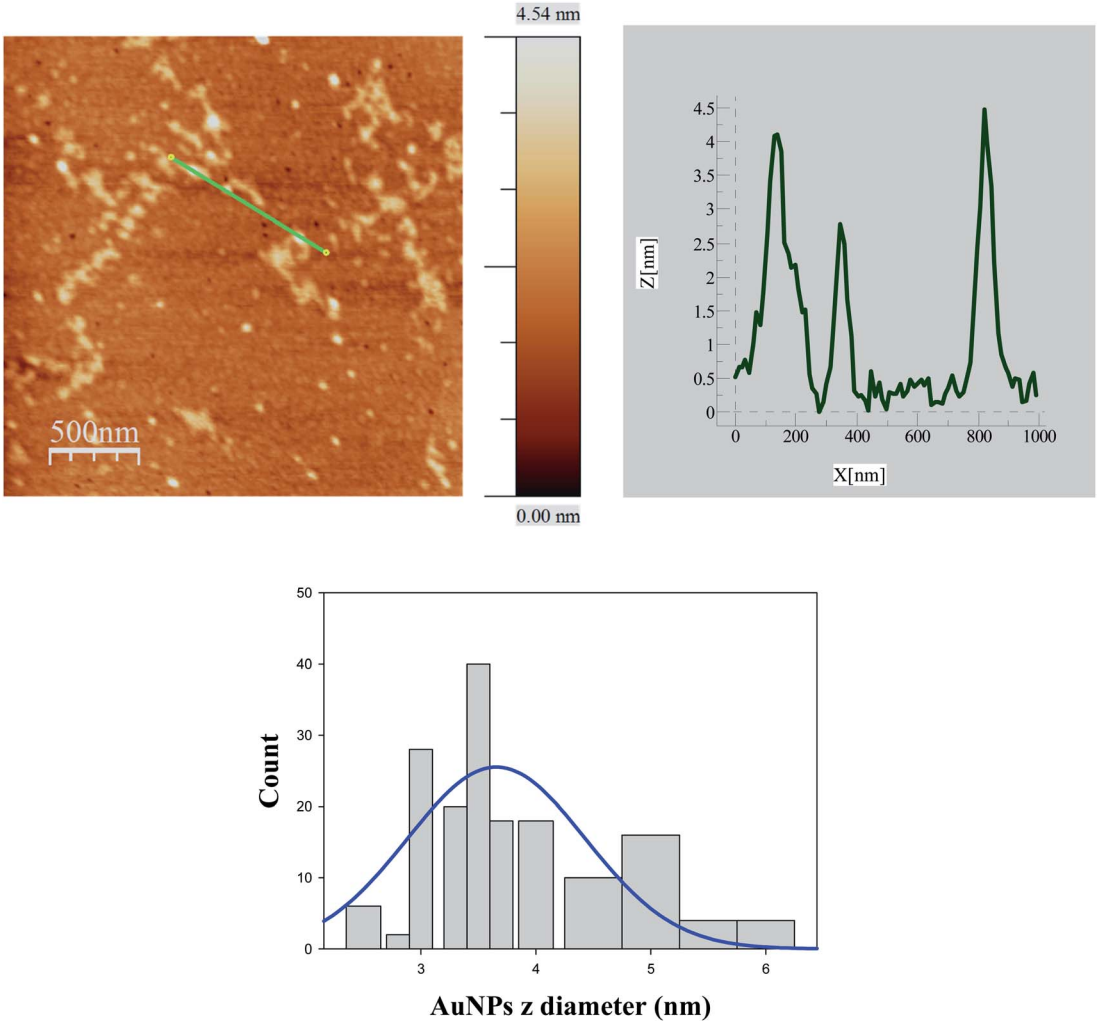

Fig. 6 AFM image for 1.0×10^{-8} M [Au@tiopronin] in the presence of $[Ru(bpy)_3]^{2+}$ and corresponding histogram from which the average diameter obtained was 3.7 ± 0.6 nm.

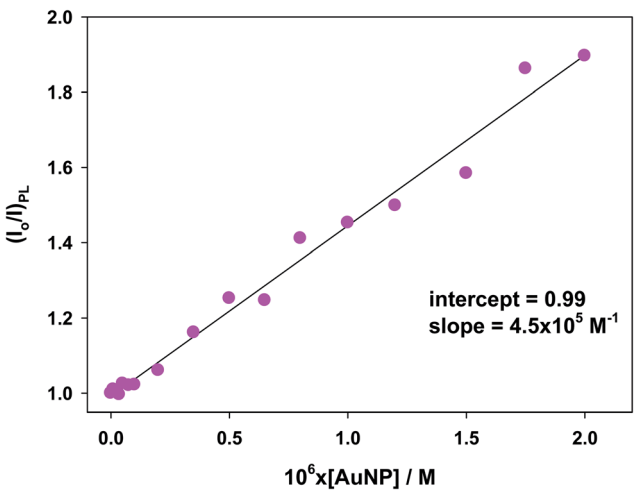

Fig. 7 Stern–Volmer plot for $[Ru(bpy)_3]^{2+}$* species in several solutions of gold nanoparticles in cacodylate buffer at pH 7.0.

augmentation of I_{ECL} and Φ_{ECL} occurs when the [AuNPs] increases. This behaviour, the ECL-enhancement effect, can be explained by the fact that the photoluminescent coupling effect (see Section 3.5) between the emission bands of the $[Ru(bpy)_3]^{2+}$* and AuNP* species (*vide infra*) is more effective than the quenching effect in this concentration range.

The physical meaning of the ECL-enhancement effect in the $[Ru(bpy)_3]^{2+}$/Au@tiopronin system will be better understood if several global processes (5)–(9) are taken into account. In simple terms, these give rise to the ECL pathway in the presence of Au@tiopronin nanoparticles. If we consider only that the free metal complex contributes to the ECL reaction (see Fig. S1,† suggesting that the ECL reaction could follow the same mechanism in the absence as well as in the presence of NPs) these processes are:

$$[Ru(bpy)_3]^{2+} + C_2O_2^{2-} \rightarrow [Ru(bpy)_3]^{2+}* \rightarrow h\vartheta] \quad (5)$$

$$[Ru(bpy)_3]^{2+}* + AuNP \rightarrow [Ru(bpy)_3]^{2+} + AuNP* \quad (6)$$

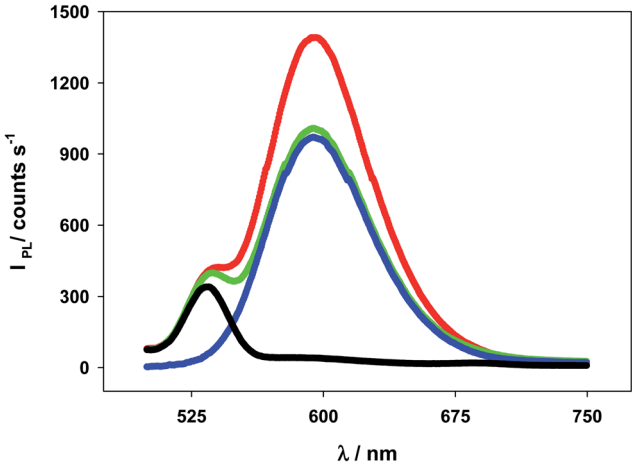

Fig. 8 Photoluminescent spectra showing the coupling effect between the emission spectra of the $[Ru(bpy)_3]^{2+}$* and AuNP* excited species. Red, coupling spectrum. Blue, $[Ru(bpy)_3]^{2+}$* spectrum. Black, AuNP* spectrum. Green, sum of the $[Ru(bpy)_3]^{2+}$* and AuNP* spectra. 4.0×10^{-7} M $[Ru(bpy)_3]^{2+}$, 1.0×10^{-8} M [AuNPs], cacodylate buffer pH 7.0.

$$\text{AuNP}^* \rightsquigarrow \text{AuNP} \quad (7)$$

$$\text{AuNP}^* \rightarrow \text{AuNP}^* \text{ (induced band)} \quad (8)$$

$$[Ru(bpy)_3]^{2+} + \text{AuNP}^* \text{ (induced band)} \rightarrow \text{AuNP} + [Ru(bpy)_3]^{2+}* \rightarrow h\vartheta \quad (9)$$

where eqn (5) represents the overall ECL reaction, equal to that taking place in the absence of NPs (the mechanism given in ref. 53 is assumed). Eqn (6) and (7) symbolize a non-reactive dynamic quenching process: the first, a non-radiative energy transfer process, involves the sensitization of an AuNP; the second denotes a non-radiative loss of energy from AuNP*. Eqn (8) indicates the generation of an induced band from sensitized AuNP* species. Finally, eqn (9) represents the enhancement of ECL emission: a radiative energy transfer which may increase the emission intensity of the emitting species, $[Ru(bpy)_3]^{2+}$*, because the photons already emitted are recaptured through the AuNP*-induced band.

Certainly, processes (7) and (8) compete with each other; though, the latter process could be favoured when the quenching effect is insignificant, as is the case in dilute solutions (see Section 3.4) and in the absence of the NPs self-aggregation (see Section 3.3); that is the case when the intermolecular interactions are negligible.[5] Furthermore, the resonance requirement for energy transfer from Ru* to NP species must be met, this condition is satisfied in our case as verified *via* the coupling measurements (see Fig. 8). Consequently, the effective coupling between both bands (ECL-Ru* emission and induced-NP*) is an essential requirement for the improvement in ECL to occur. Therefore, the ECL-enhancement in the diluted range of the NPs can be rationalized by the ECL-Ru*-induced-NP* coupling effect or nanoparticle-induced resonance transfer (NP-RET) effect. In order to quantify the NP-RET effect on the $[Ru(bpy)_3]^{2+}$/Au@tiopronin system using an ECL reaction, eqn (10) was applied for the diluted range:

$$\frac{\Phi_{ECL}}{\Phi^o_{ECL}} = 1 + K_{(\text{NP-RET})_{ECL}}[\text{AuNP}] \quad (10)$$

where, $K_{(\text{NP-RET})_{ECL}}$ denotes the NP-RET effectiveness (defined as the efficacy of a nanoparticle to increase the emission of an ECL reaction by resonance energy transfer), and Φ_{ECL} and Φ^o_{ECL} account for the ECL efficiencies for the actual and standard reactions, respectively (see Section 3.1). Explicitly, $K_{(\text{NP-RET})_{ECL}}$ quantifies how much an ECL reaction has been enhanced. Fig. 9 shows a plot for eqn (10): from the slope, a value of 1.2×10^7 M^{-1} is found for $K_{(\text{NP-RET})_{ECL}}$, being about 28 times higher than K_Q for the system $[Ru(bpy)_3]^{2+}$/Au@tiopronin.

In addition, an estimate of the photoluminescent coupling constant $K_{(\text{NP-RET})_{PL}}$ can be made by:

$$\frac{\left(\frac{I}{I_o}\right)_{PL} - 1}{[\text{AuNP}]} = K_{(\text{NP-RET})_{PL}} \quad (11)$$

I and I_o being the intensities at the emission maximum of the photoluminescent spectra for coupled and uncoupled Ru(II)* species, respectively. Through the emission spectra of Fig. 8, the value for $K_{(\text{NP-RET})_{PL}}$ was 4.3×10^7 M^{-1}, in agreement with the result achieved from ECL measurements.

Therefore, in diluted NP solutions the observed ECL increase is due to an NP-RET effect that surpasses the quenching effect. We must emphasize that the NP-RET effect is only operative in diluted solutions in which the aggregation phenomenon does not occur.

Returning to the ECL-detraction result for the concentrated range of NPs, this is easily understood through the combined action of the quenching and NPs self-aggregation effects. Assuming that only the free metal complex contributes to the ECL reaction as previously mentioned, and bearing in mind eqn

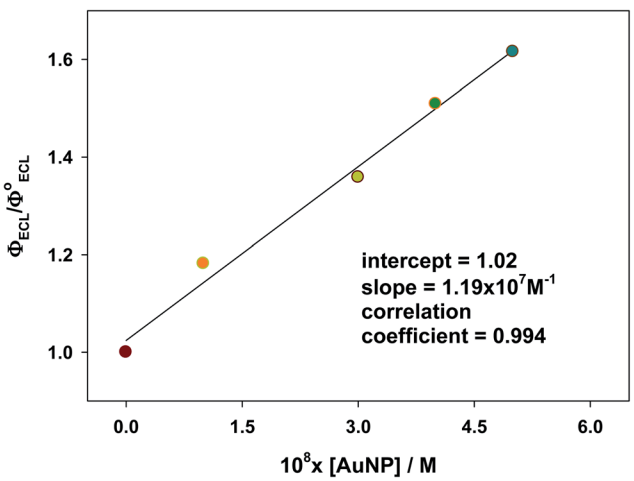

Fig. 9 Relative ECL efficiency plotted *vs.* AuNPs concentration showing the NP-RET effectiveness of the $[Ru(bpy)_3]^{2+}$/Au@tiopronin system. Cacodylate buffer, pH 7.0.

(5) and (9) as the only sources of the emission energy, two phenomena can lead to a decrease in the light emission: on one hand, static quenching, which would begin to be significant together with dynamic quenching; and on the other, the self-aggregation that would decrease the number of free NPs. The first would cause a decrease in the available $[Ru(bpy)_3]^{2+}$ species for ECL reaction; the second by decreasing the number of free NPs also decreases the probability that reactions (6)–(9) of the previously proposed mechanism can occur. If this last effect were predominant, I_{ECL} and Φ_{ECL} should reach a constant value by increasing the concentration of AuNPs, which does not occur. Therefore, in the concentrated range of NPs both I_{ECL} and Φ_{ECL} decrease as a consequence of the combined action of the self-aggregation and the static quenching effects, causing a decrease in free NPs and available $[Ru(bpy)_3]^{2+}$ species for ECL reaction, respectively.

5. Conclusions

ECL efficiencies, redox potentials, PL quenching and coupling effects, and AFM photograms of the $[Ru(bpy)_3]^{2+}$/Au@tiopronin system were determined in several aqueous solutions of AuNPs. The most remarkable finding was that ECL measurements can display the nanoparticle-induced resonance energy transfer (NP-RET) effect. Its effectiveness was quantified through a coefficient, $K_{(NP\text{-}RET)_{ECL}}$, which measures how much an ECL reaction has been enhanced. Moreover, it should also be noted that the NP-RET effect was also verified through PL measurements, in such a way that a coefficient, $K_{(NP\text{-}RET)_{PL}}$, was determined, both constants, $K_{(NP\text{-}RET)_{ECL}}$ and $K_{(NP\text{-}RET)_{PL}}$ being in close agreement. We must highlight the fact that the NP-RET effect is only displayed in diluted solutions in which there is no NPs self-aggregation. The existence of the NPs self-aggregation behavior is revealed through AFM measurements.

Conflicts of interest

There are no conflicts to declare.

Acknowledgements

This work was financed by the Universidad de Sevilla, 2017/00001066 (18.04.03.1602) and 2018//00000502-1804031703, as well Junta de Andalucia 1804032996/2017-2018/00000810. We thank CITIUS, Universidad de Sevilla for its assistance in obtaining TEM and AFM images.

Notes and references

1 A. Aguila and R. W. Murray, Monolayer-Protected Clusters with Fluorescent Dansyl Ligands, *Langmuir*, 2000, **16**, 5949–5954.
2 T. Huang and R. W. Murray, Quenching of $[Ru(bpy)_3]^{2+}$ Fluorescence by Binding to Au Nanoparticles, *Langmuir*, 2002, **18**, 7077–7081.
3 G. Mandal, M. Bardhan and T. Ganguly, Occurrence of Forster Resonance Energy Transfer between Quantum Dots and Gold Nanoparticles in the Presence of a Biomolecule, *J. Phys. Chem. B*, 2011, **115**, 20840–20848.
4 A. L. Rodarte and A. R. Tao, Plasmon–Exciton Coupling between Metallic Nanoparticles and Dye Monomers, *J. Phys. Chem. C*, 2017, **121**, 3496–3502.
5 P. Klán and J. Wirz, *Photochemistry of Organic Compounds: From Concepts to Practice*, John Wiley & Sons, Chichester-West Sussex, United Kingdom, 2009, ch. 2.
6 G. Bunt and F. S. Wouters, FRET from single to multiplexed signaling events, *Biophys. Rev.*, 2017, **9**, 119–129.
7 A. Iqbal, S. Arslan, B. Okumus, T. J. Wilson, G. Giraud, D. G. Norman, T. Ha and D. M. J. Lilley, Orientation dependence in fluorescent energy transfer between Cy3 and Cy5 terminally attached to double-stranded nucleic acids, *Proc. Natl. Acad. Sci. U. S. A.*, 2008, **105**, 11176–11181.
8 P. Rajdev and S. Ghosh, Fluorescence Resonance Energy Transfer (FRET): A Powerful Tool for Probing Amphiphilic Polymer Aggregates and Supramolecular Polymers, *J. Phys. Chem. B*, 2019, **123**, 327–342.
9 E. Haustein, M. Jahnz and P. Schwille, Triple FRET: A tool for Studying Long-Range Molecular Interactions, *ChemPhysChem*, 2003, **4**, 745–748.
10 L. Olejko, P. J. Cywinski and I. Bald, An ion-controlled four-color fluorescent telomeric switch on DNA origami structures, *Nanoscale*, 2016, **8**, 10339–10347.
11 C. M. Spillmann, S. Buckhout-White, E. Oh, E. Goldman, R. M. G. Ancona and I. L. Medintz, Extending FRET cascades on linear DNA photonic wires, *Chem. Commun.*, 2014, **50**, 7246–7249.
12 S. Saini, H. Singh and B. Bagchi, Fluorescence resonance energy transfer (FRET) in chemistry and biology: Non-Förster distance dependence of the FRET rate, *J. Chem. Sci.*, 2006, **118**, 23–35.
13 S. Sutradhar and S. Patnaik, Structure and Dynamics of a *N*-Methylfulleropyrrolidine-Mediated Gold Nanocomposite: A Spectroscopic Ruler, *ACS Appl. Mater. Interfaces*, 2017, **9**, 21921–21932.
14 C. S. Yun, A. Javier, T. Jennings, M. Fisher, S. Hira, S. Peterson, B. Hopkins, N. O. Reich and G. F. Strouse, Nanometal Surface Energy Transfer in Optical Rulers, Breaking the FRET Barrier, *J. Am. Chem. Soc.*, 2005, **127**, 3115–3119.
15 P. C. Ray, Z. Fan, R. A. Crouch, S. S. Sinha and A. Pramanik, Nanoscopic optical rulers beyond the FRET distance limit: fundamentals and applications, *Chem. Soc. Rev.*, 2014, **43**, 6370–6404.
16 A. I. Chizhik, J. Rother, I. Gregor, A. Janshoff and J. Enderlein, Metal-induced energy transfer for live cell nanoscopy, *Nat. Photonics*, 2014, **8**, 124–127.
17 G. Zengin, T. Gschneidtner, R. Verre, L. Shao, T. J. Antosiewicz, K. Moth-Poulsen, M. Käll and T. Shegai, Evaluating Conditions for Strong Coupling between Nanoparticle Plasmons and Organic Dyes Using Scattering and Absorption Spectroscopy, *J. Phys. Chem. C*, 2016, **120**, 20588–20596.
18 J.-M. Jung, H.-W. Yoo, F. Stellacci and H.-T. Jung, Two-Photon Excited Fluorescence Enhancement for

Ultrasensitive DNA Detection on Large-Area Gold Nanopatterns, *Adv. Mater.*, 2010, **22**, 2542–2546.

19 G. Haran and L. Chuntonov, Artificial Plasmonic Molecules and their Interaction with Real Molecules, *Chem. Rev.*, 2018, **118**, 5539–5580.

20 R. Chikkaraddy, B. de Nijs, F. Benz, S. J. Barrow, O. A. Scherman, E. Rosta, A. Demetriadou, P. Peter Fox, O. Hess and J. J. Baumberg, Single-Molecule Strong Coupling at Room Temperature in Plasmonic Nanocavities, *Nature*, 2016, **535**, 127–130.

21 J.-L. Yang, J. Xu, H. Ren, L. Sun, Q.-C. Xu, H. Zhang, J.-F. Li and Z.-Q. Tian, In Situ SERS Study of Surface Plasmon Resonance Enhanced Photocatalytic Reactions using Bifunctional Au@CdS Core-Shell Nanocomposites, *Nanoscale*, 2017, **9**, 6254–6258.

22 Z. Liu, W. Hou, P. Pavaskar, M. Avkol and S. B. Cronin, Plasmon Resonant Enhancement of Photocatalytic Water Splitting Under Visible Illumination, *Nano Lett.*, 2011, **11**, 1111–1116.

23 X. You, S. Ramakrishna and T. Seideman, Plasmon-Mediated Absorption and Photocurrent Spectra in Sensitized Solar Cells, *ACS Photonics*, 2017, **4**, 1178–1187.

24 S. Cerfontaine, L. Lionel Marcélis, B. Laramee-Milette, G. S. Hanan, F. Loiseau, J. De Winter, P. Gerbaux and B. Elias, Converging Energy Transfer in Polynuclear Ru(II) Multiterpyridine Complexes: Significant Enhancement of Luminescent Properties, *Inorg. Chem.*, 2018, **57**, 2639–2653.

25 C. Caucheteur, T. Go and J. Albert, Review of Plasmonic Fiber Optic Biochemical Sensors: Improving the Limit of Detection, *Anal. Bioanal. Chem.*, 2015, **407**, 3883–3897.

26 Y. Bao, E. Guégain, V. Nicolas and J. Nicolas, Fluorescent Polymer Prodrug Nanoparticles with Aggregation-Induced Emission (AIE) Properties from Nitroxide-Mediated Polymerization, *Chem. Commun.*, 2017, **53**, 4489–4492.

27 G. Cai, Z. Yu, R. Ren and D. Tang, Exciton–Plasmon Interaction between AuNPs/Graphene Nanohybrids and CdS Quantum Dots/TiO_2 for Photoelectrochemical Aptasensing of Prostate-Specific Antigen, *ACS Sens.*, 2018, **3**, 632–639.

28 W. Miao, Electrogenerated Chemiluminescence and Its Biorelated Applications, *Chem. Rev.*, 2008, **108**, 2506–2553.

29 K. M. Omer, S.-Y. Ku, K.-T. Wong and A. J. Bard, Green Electrogenerated Chemiluminescence of Highly Fluorescent Benzothiadiazole and Fluorene Derivatives, *J. Am. Chem. Soc.*, 2009, **131**, 10733–10741.

30 E. K. Walker, D. A. V. Bout and K. J. Stevenson, Aqueous Electrogenerated Chemiluminescence of Self-Assembled Double-Walled Tubular J-Aggregates of Amphiphilic Cyanine Dyes, *J. Phys. Chem. C*, 2011, **115**, 2470–2475.

31 T. Joshi, G. J. Barbante, P. S. Francis, C. F. Hogan, A. M. Bond, G. Gasser and L. Spiccia, Electrochemiluminescent Monomers for Solid Support Syntheses of Ru(II)-PNA Bioconjugates: Multimodal Biosensing Tools with Enhanced Duplex Stability, *Inorg. Chem.*, 2012, **51**, 3302–3315.

32 W.-W. Zhao, J. Wang, Y.-C. Zhu, J.-J. Xu and H.-Y. Chen, Quantum Dots: Electrochemiluminescent and Photoelectrochemical Bioanalysis, *Anal. Chem.*, 2015, 9520–9531.

33 F.-R. F. Fan and A. J. Bard, Observing Single Nanoparticle Collisions by Electrogenerated Chemiluminescence Amplification, *Nano Lett.*, 2008, **8**, 1746–1749.

34 Z. Ding, B. M. Quinn, S. Haram and A. J. Bard, Electrochemistry and Electrogenerated Chemiluminescence from Silicon Nanocrystal Quantum Dots, *Science*, 2002, **296**, 1293–1297.

35 J. Rodríguez-López, M. Shen, A. B. Nepomnyashchii and A. J. Bard, Scanning Electrochemical Microscopy Study of Ion Annihilation Electrogenerated Chemiluminescence of Rubrene and $[Ru(bpy)_3]^{2+}$, *J. Am. Chem. Soc.*, 2012, **134**, 9240–9250.

36 Z. Chen, Y. Liu, Y. Wang, X. Zhao and J. Li, Dynamic Evaluation of Cell Surface *N*-Glycan Expression *via* an Electrogenerated Chemiluminescence Biosensor Based on Concanavalin A-Integrating Gold-Nanoparticle-Modified $Ru(bpy)_3^{2+}$-Doped Silica Nanoprobe, *Anal. Chem.*, 2013, **85**, 4431–4438.

37 A. Poulpiquet, B. D. Buitrago, M. D. Milutinovic, M. Sentic, S. Arbault, L. Bouffier, A. Kuhn and N. Sojic, Dual Enzymatic Detection by Bulk Electrogenerated Chemiluminescence, *Anal. Chem.*, 2016, **88**, 6585–6592.

38 H.-R. Zhang, Y.-Z. Wang, W. Zhao, J.-J. Xu and H.-Y. Chen, Visual Color-Switch Electrochemiluminescence Biosensing of Cancer Cell Based on Multichannel Bipolar Electrode Chip, *Anal. Chem.*, 2016, **88**, 2884–2890.

39 C. Duan, H. Cui, Z. Zhang, B. Liu, J. Guo and W. Wang, Size-Dependent Inhibition and Enhancement by Gold Nanoparticles of Luminol-Ferricyanide Chemiluminescence, *J. Phys. Chem. C*, 2007, **111**, 4561–4566.

40 Z. Li, Z. Lin, X. Wu, H. Chen, Y. Chai and R. Yuan, Highly Efficient Electrochemiluminescence Resonance Energy Transfer System in One Nanostructure: Its Application for Ultrasensitive Detection of MicroRNA In Cancer Cells, *Anal. Chem.*, 2017, **89**, 6029–6035.

41 J. Wang, Y. Shan, W.-W. Zhao, J.-J. Wu and H.-Y. Chen, Gold Nanoparticle Enhanced Electrochemiluminescence of CdS Thin Films for Ultrasensitive Thrombin Detection, *Anal. Chem.*, 2011, **83**, 4004–4011.

42 H. Wang, Y. Yuan, Y. Zhuo, Y. Chai and R. Yuan, Self-Enhanced Electrochemiluminescence Nanorods of Tris(bipyridine) Ruthenium(II) Derivative and Its Sensing Application for Detection of *N*-Acetyl-β-D-glucosaminidase, *Anal. Chem.*, 2016, **88**, 2258–2265.

43 In a previous work (P. Perez-Tejeda, E. Grueso, A. Marin-Gordillo, C. Torres-Marquez and R. M. Giráldez-Pérez, *ACS Appl. Nano Mater.*, 2018, **1**, 5307–5315) the ECL efficiency of the $[Ru(bpy)_3]^{2+}/C_2O_4^{2-}$ reaction was determined in the presence of citrate-coated gold (Au@citrate) nanoparticle aqueous solutions. In this system it was observed that ECL measurements displayed the emission-SPR coupling effect in diluted and aggregated solutions of the Au@citrate NPs. In fact, this effect is a result of the sufficiently strong electrostatic $[Ru(bpy)_3]^{2+}$/Au@citrate binding, causing

a metal nanostructure in solution which is revealed by TEM and EDS measurements.

44 R. Prado-Gotor and E. Grueso, A kinetic study of the interaction of DNA with gold nanoparticles: mechanistic aspects of the interaction, *Phys. Chem. Chem. Phys.*, 2011, **13**, 1479–1489.

45 A. C. Templeton, S. Chen, S. M. Gross and R. W. Murray, Water-soluble, isolable gold clusters protected by tiopronin and coenzyme a monolayers, *Langmuir*, 1999, **15**, 66–76.

46 The self-aggregation is a function of the medium pH. In this way, the higher the pH, the less aggregation. Information obtained from experiments carried out in the authors' laboratory.

47 P. Perez-Tejeda, R. Prado-Gotor and E. M. Grueso, Electrochemiluminescence (ECL) of the $[Ru(bpy)_3]^{2+}$ Complex: The Coreactant Effect of PAMAM Dendrimers in an Aqueous Medium, *Inorg. Chem.*, 2012, **51**, 10825–10831.

48 A. Jimenez-Ruiz, E. Grueso and P. Perez-Tejeda, Electrogenerated Chemiluminescence Reactions Between the $[Ru(bpy)_3]^{2+}$ Complex and PAMAM GX.0 Dendrimers in an Aqueous Medium, *J. Inorg. Biochem.*, 2015, **151**, 18–25.

49 A. Jimenez-Ruiz, E. Grueso, P. Perez-Tejeda, F. Muriel-Delgado and C. Torres-Marquez, Electrochemiluminescent (ECL) $[Ru(bpy)_3]^{2+}$/PAMAM Dendrimer Reactions: Coreactant Effect and 5-Fluorouracil/Dendrimer Complex Formation, *Anal. Bioanal. Chem.*, 2016, **408**, 7213–7217.

50 R. D. Mussell and D. G. Nocera, Effect of Long-Distance Electron Transfer on Chemiluminescence Efficiencies, *J. Am. Chem. Soc.*, 1988, **110**, 2764–2772.

51 A. Kapturkiewicz, *Electrogenerated Chemiluminescence*, ed. A. J. Bard, Marcel Dekker, New York, 2004, ch. 4.

52 M. M. Richter, Electrochemiluminescence (ECL), *Chem. Rev.*, 2004, **104**, 3003–3036.

53 F. Kanoufi and A. Bard, Electrogenerated Chemiluminescence. 65. An Investigation of the Oxidation of Oxalate by Tris(polypyridine) Ruthenium Complexes and the Effect of the Electrochemical Steps on the Emission Intensity, *J. Phys. Chem. B*, 1999, **103**, 10469–10480.